Correlated fluorescence and 3D electron microscopy with high sensitivity and spatial precision

Wanda Kukulski,[1,2] Martin Schorb,[1] Sonja Welsch,[1] Andrea Picco,[2] Marko Kaksonen,[2] and John A.G. Briggs[1,2]

[1]Structural and Computational Biology Unit and [2]Cell Biology and Biophysics Unit, European Molecular Biology Laboratory, D-69117 Heidelberg, Germany

Correlative electron and fluorescence microscopy has the potential to elucidate the ultrastructural details of dynamic and rare cellular events, but has been limited by low precision and sensitivity. Here we present a method for direct mapping of signals originating from ~20 fluorescent protein molecules to 3D electron tomograms with a precision of less than 100 nm. We demonstrate that this method can be used to identify individual HIV particles bound to mammalian cell surfaces. We also apply the method to image microtubule end structures bound to mal3p in fission yeast, and demonstrate that growing microtubule plus-ends are flared in vivo. We localize Rvs167 to endocytic sites in budding yeast, and show that scission takes place halfway through a 10-s time period during which amphiphysins are bound to the vesicle neck. This new technique opens the door for direct correlation of fluorescence and electron microscopy to visualize cellular processes at the ultrastructural scale.

Introduction

Electron microscopy (EM), and more recently electron tomography (ET), are important tools in cell biology, providing detailed information about cellular ultrastructures, membrane shapes, and organelle architecture. Nevertheless, certain cellular features and events have remained difficult or impossible to address using EM. Small, rare, or transient steps in dynamic processes are difficult to locate in EM within the enormous volume of a cell or group of cells. Even if such features can be occasionally located, a meaningful quantitative analysis requires observation of multiple copies of a rare event. Unknown structures with no described morphological characteristics, or those that are similar to other related structures, can be hard to distinguish. Knowledge of the protein composition may also be required, for example when attempting to understand the structural differences between two features in the presence or absence of a particular protein. All of these problems are exacerbated when there is a need to collect 3D ET data of thick samples, which are difficult to visually screen or label with antibodies. These problems have left a gap in our understanding of many fundamental cellular events and processes in the critical 1–100-nm resolution range.

Fluorescence light microscopy (FM) is ideal for the localization of rare and dispersed structures within the cell. It reveals the protein dynamics that underlie formation and progression of such structures. Using multiple fluorescent labels, it is possible to distinguish similar structures or transient intermediates according to the presence or absence of specific components. Clearly, a significant number of important cell biological questions could be addressed if the location and momentary local protein composition of a cellular event, as determined by FM, could subsequently be used to identify and visualize the very same event by 3D ultrastructural EM.

A method to achieve this goal must fulfill a number of additional methodological requirements. First, the method must be solidly reproducible. Second, it must be possible to locate the feature of interest in the electron micrograph with a spatial precision that is appropriate for ultrastructure studies (of the order of 100 nm), and with a defined localization error. Third, the method should be sensitive enough to allow detection of faint fluorescent signals that originate from proteins present at low copy numbers. Fourth, it should permit the simultaneous use of differently colored fluorescent proteins (FPs). Finally, the method should ideally be applicable to a broad range of organisms and cell types.

Correspondence to John A.G. Briggs: briggs@embl.de; or Marko Kaksonen: kaksonen@embl.de

Abbreviations used in this paper: ET, electron tomography; FM, fluorescence light microscopy; FP, fluorescent protein; FS, freeze substitution; HIV, human immunodeficiency virus; HPF, high pressure freezing; MT, microtubule; SPB, spindle pole body.

Currently available correlative microscopy methods have shown to be valuable tools for tracing back cells of interest within an organism or identifying fluorescently labeled organelles (Müller-Reichert et al., 2007; van Rijnsoever et al., 2008; Verkade, 2008; Kolotuev et al., 2009; Nixon et al., 2009; van Driel et al., 2009; and Discussion). However, the high level of precision and sensitivity necessary to answer questions about small subcellular features, where EM can be most informative, has not yet been reached with these approaches.

Here we present a simple, robust, correlative FM and EM method that meets all the requirements outlined above. It allows multi-color imaging of conventional fluorescent fusion proteins with high sensitivity (∼20 copies of a FP). The same features can then be localized with high precision (<100 nm) within a 3D volume by ET. We provide evidence of the robustness and the methodological significance of our approach by applying the method to three different, biologically significant systems, thereby aiming at morphologically and functionally diverse ultrastructures identified by both GFP- and RFP-labeled proteins.

Directly correlating FM and ET data at a high level of precision and sensitivity provides a new opportunity to obtain the missing information on the 1–100-nm scale that is needed to answer important cell biological problems. Defined time points of dynamic, rare, or structurally undescribed events can be identified and their ultrastructure described in 3D.

Results

Simultaneous preservation of fluorescent signals and ultrastructure

To ensure that the same time point is imaged in both the FM and EM image, and to minimize any positional changes between the FM and the EM images, we wished to image the fluorescence signal after preparation of the sample for EM. To retain fluorescent signals in resin-embedded cells, we began by adapting the protocol described in Nixon et al. (2009), consisting of cryofixation, freeze substitution (FS), and embedding in Lowicryl resin. We optimized the protocol for structure preservation and FP signal retention (see Materials and methods). For FM and subsequent ET, 300-nm sections were cut from resin-embedded samples and placed on carbon-coated EM grids.

To assess the preservation of the FP signal, *Saccharomyces cerevisiae* cells expressing EGFP- and mCherry-tagged endocytic proteins were subjected to live-cell FM, and were also cryofixed, embedded, and sectioned. We compared the fluorescent signal in images of 300-nm resin sections with corresponding images from live-cell imaging (Fig. 1, A–D). In both cases, fluorescent signals from EGFP and mCherry were detected, as well as colocalizing spots. In wide-field live-cell microscopy, spots are visible over a focal range of ∼1 μm, while sections are only 300 nm thick. We therefore expected sectioned cells to exhibit about one third of the number of fluorescent spots observed in live-cell microscopy. The observed signal distribution corresponded well to that estimation (Fig. 1, B and D), indicating that the majority of fluorescent signals are retained.

The average number of FP copies at the fluorescent endocytosis patches was determined from live-cell imaging against a reference system based on the method described in Joglekar et al. (2006) (unpublished data). Fig. 1 shows preservation of the fluorescence signal in Lowicryl sections from both EGFP- and mCherry-tagged versions of the endocytic protein Sla1, which has an average copy number of 25 per fluorescent spot. In each case, fluorescent Sla1 was expressed in combination with actin-binding protein Abp1, which is present in average at 85 copies, tagged with the respective other FP. Even in the case of Rvs167-EGFP, where the signal derives from an average of 21 molecules, fluorescence could be still routinely detected (Fig. S1). Comparison of live-cell and section images shows that the signal-to-background ratio in sections is similar to that in live-cell imaging. As in live-cell imaging, the lower limit of detection for FP signals is determined by parameters including the cytosolic background of the tagged protein and the sharpness of the protein patch. We conclude that the embedding procedure preserves the vast majority of the fluorescent signal, and that for proteins giving low levels of cytosolic background, the detection of signals at copy numbers even lower than 21 would be possible.

The successful preservation of fine ultrastructure in different cells is shown in Fig. 1, E and F, illustrating the spindle pole body (SPB) and MTs as well as membranous structures such as the plasma membrane or the nuclear envelope in *S. cerevisiae* (Fig. 1 E) and in MDCK cells (Fig. 1 F), in which also the actin cytoskeleton in filopodia was preserved. The preservation compares well with other recent ET studies of Lowicryl-embedded cells (Höög et al., 2007; Chlanda et al., 2009).

Transferring the sample between the FM and the EM, and low precision initial correlation

To routinely perform reproducible, quantitative correlation, resin sections imaged by FM must be transferred to the EM in an easy and reliable way with virtually no loss or damage of imaged areas. This robustness must be compatible with the ability to perform high end FM and ET on the very same areas. To achieve this, we image resin sections by FM in water, after their deposition on the EM grid, using high NA oil-immersion objectives (see Materials and methods and Fig. S2). The EM grid can be recovered after FM imaging without any damage. At this point, it is possible to apply standard procedures such as addition of gold fiducials or further contrast enhancement by post-staining of sections, if desired. The grid is then inserted into the EM, the regions previously imaged by FM are targeted, and cells of interest can be found back by their position relative to the bars of the EM grid.

High precision correlation

To unambiguously locate a small ultrastructural detail of potentially unknown structure based on its fluorescent signal, it is next necessary to predict its location within the cell with high precision. A procedure that aims at high precision correlation needs to deal with several potential problems: the considerable change of field of view and resolution between FM and EM, the lack of visual guidelines within a 300-nm section, and the nonuniform distortions that occur in EM sections due to exposure to the electron beam (Luther et al., 1988). To deal with

Live cell   **300nm resin section**

A   B

25 x EGFP
85 x mCherry

C   D

85 x EGFP
25 x mCherry

E

F
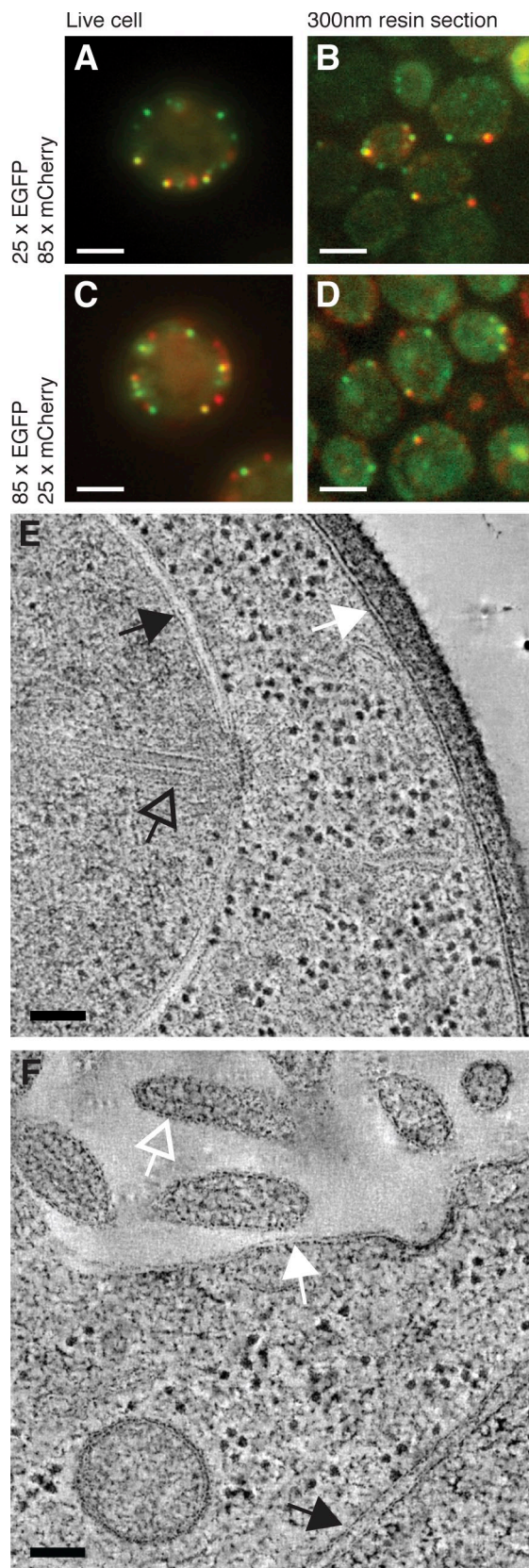
Figure 1. **Preservation of fluorescence and ultrastructure.** Preservation of fluorescent protein signals tagged to endocytic proteins in *S. cerevisiae*. (A and B) Sla1-EGFP/Abp1-mCherry, (C and D) Sla1-mCherry/Abp1-EGFP. Left panels (A and C) are live-cell fluorescence microscopy images, right panels (B and D) are fluorescent microscopy images of 300-nm resin sections on EM grids. (E and F) Slices through electron tomograms show preservation of fine structure in *S. cerevisiae* (E) and MDCK cells (F). Both were subjected to cryo-immobilization by HPF, FS with 0.1% uranyl acetate in acetone, and low-temperature embedding in Lowicryl resin. Example features are marked: the plasma membrane (white arrows), nuclear envelope (black arrows), cytoskeletal elements such as spindle pole body and nuclear microtubuli (black open arrow), and filopodia (white open arrow). Bars: (A–D) 2 µm; (E and F) 100 nm.

these difficulties, our correlation procedure uses small fluorescent microspheres that are visible both by FM and ET as fiducial markers. The spheres are added to the section before FM, and imaged in a fluorescence channel separate from that of the FPs of interest (Fig. 2, A and B). By ET, the spheres can be easily seen on the section surface within the reconstructed tomographic volume (Fig. 2 C). The coordinates of the centroid of each fiducial marker are measured in the FM image and the EM image (Fig. 2, B and C). These coordinates are used to directly calculate the optimal transformation between the two images. This transformation takes into account changes in magnification, rotation, and distortions due to the electron beam. The same transformation is then applied to the centroid coordinates of the FP signal of interest, defining its coordinates within the tomogram (Fig. 2 D and Materials and methods).

The use of fiducial markers for correlation provides a robust coordinate system that allows a position from the FM image to be located within the EM image with a precision on the "tens of nms" scale (see below). The set of fiducial beads that is used to calculate the transform is large enough to absorb small errors in single fiducial bead positioning. The precision is therefore usually limited by the accuracy with which the centroid of the fluorescent spot of interest can be determined: sub-pixel errors in the FM image translate into large errors in the positioning within the EM image. For this reason it is also necessary to consider potential movements or distortions between the FM images of the fluorescent channel containing the fiducials and the channel containing the signal of interest. These can result from drift of the microscope stage between the two images or chromatic aberration of the FM objective. These problems can be overcome by eliminating the source of the movements or distortions, or by measuring and correcting for them (see Materials and methods).

Accuracy of correlation and error estimation

To estimate how accurate the correlation is, we made use of the sets of fiducials that are used to calculate the transforms. By excluding one fiducial from the calculation of the transform we were instead able to treat it as the object of interest and predict its position within the tomogram. The calculated position could then be compared with the actual position at which the bead was seen in the tomogram, to determine the error of the prediction. By repeating this calculation for all fiducials across all tomograms in the dataset, it was possible to obtain a direct readout of the correlation accuracy of the system. This analysis was performed separately for three datasets: *Schizosaccharomyces pombe*, *S. cerevisiae*, and MDCK cells (see below). We found
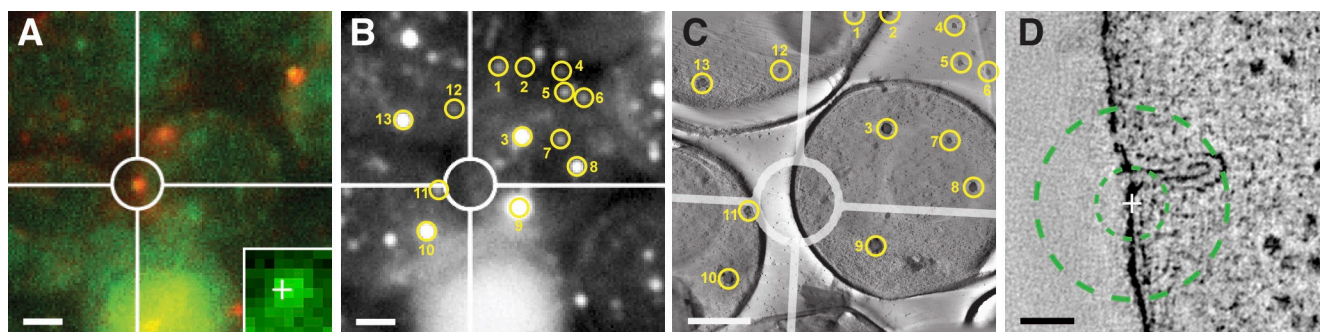
Figure 2. Correlation procedure based on fiducials. (A) Merge of GFP and RFP channels of Rvs167-EGFP/Abp1-mCherry expressed in *S. cerevisiae*. The patch of interest is highlighted by the circle. Inset shows the Rvs167-EGFP signal of that patch, boxed as for centroid fitting. A cross marks the resulting centroid position. (B) Blue FluoSpheres (365 nm/415 nm) channel. Fiducials selected for correlation are marked with yellow circles and numbers. (C) Same fiducials as in B present on merged slices of the section surface from a tomogram of the cell of interest are assigned to the corresponding fluorescent spots in the FM image (marked by yellow circles and numbers). White circle and guidelines correspond to A and B after applying the optimal transform, calculated using the coordinates of the selected fiducials. (D) Slice of high magnification tomogram showing the endocytic invagination. Cross marks the centroid coordinates of the fluorescent patch transformed into tomogram coordinates. The inner circle corresponds to a probability radius of 50% (33 nm), outer circle to 80% (89 nm). Bars: (A–C) 1 µm; (D) 50 nm.

that 50% of positions are predicted with an accuracy of 52, 33, and 40 nm, and 80% of the fiducials are positioned within 121, 89, and 100 nm accuracy from the predicted position in the three systems. The distribution of errors for all three systems is shown in Fig. 3.

Localization of HIV particles on the surface of cells

We next wished to provide a demonstration that these error estimates are appropriate, and to illustrate the method's potential for locating small, rare features. We added HIV-1 particles labeled with MA-EGFP, and lacking the viral envelope protein that is required for virus–cell fusion (see Materials and methods and Müller et al., 2004), to adherently growing MDCK cells with RFP-labeled histone protein H2B labeling the nucleus. In this system productive viral entry cannot occur, and instead we attempted to locate virus particles at the surface of mammalian cells even when present at very low concentration. This mimics

Figure 3. Localization error plotted against the percentage of correlations. Percentage of correlated fiducials (x-axis) found within a certain distance (y-axis) of the position predicted using the optimal transformation calculated excluding that fiducial. The three curves correspond to three different datasets: MDCK cells (yellow), *S. cerevisiae* (blue), and *S. pombe* (green). Accuracies for 50% and 80% of predictions are marked with dashed and dotted lines, respectively.

the situation during studies of viral entry, where productive entry is rare and difficult to locate. In conventional FM the cellular nuclei were outlined by the RFP signal, whereas HIV particles appeared as bright GFP spots around the cell. In resin sections, we observed similarly bright GFP spots in the cell peripheries. The positions of these spots were investigated by ET (Fig. 4 A) and were found to correlate with HIV particles with a characteristic morphology. Typically, we found virus particles among filopodia-like protrusions of the cell surface (Fig. 5, A–E; Video 1).

We compared the predicted positions of 17 GFP-labeled HIV particles bound to MDCK cells with their actual positions. The centers of the 17 virus particles were found at 14–191 nm from their predicted positions; 8 of the 17 centers were found within 42 nm, 14 of the 17 within 81 nm. This distribution is consistent with the prediction that 80% and 50% of correlations have an accuracy of 100 nm and 40 nm, respectively.

Growing MT plus-ends have flared structures

Next, we wished to use the method to address open questions in cell biology. Distinct open and closed MT end structures have been described in vivo and assigned to either plus or minus ends by cellular ET (O'Toole et al., 1999, 2003; Höög et al., 2007). Because the majority of plus-end structures showed a flared morphology, it was suggested that these represent growing plus-ends, because MT growth is slower than shrinking (Höög et al., 2007). In vitro studies, however, suggest that growing MT-ends exhibit a sheet-like structure, closing to form the hollow tube (Chrétien et al., 1995). This question would be most effectively answered by an unambiguous direct correlation of the dynamic state and the end morphology of single MTs in vivo.

One group of MT-associated proteins are the MT plus-end–tracking proteins (+TIPs), which specifically bind to growing plus-ends and regulate their dynamics (Akhmanova and Hoogenraad, 2005). The +TIP mal3p is the fission yeast homologue of end-binding protein 1 (EB1), which has been shown to localize along MTs and to accumulate at growing MT plus-ends, thereby regulating MT stability and recruiting other proteins to the MT
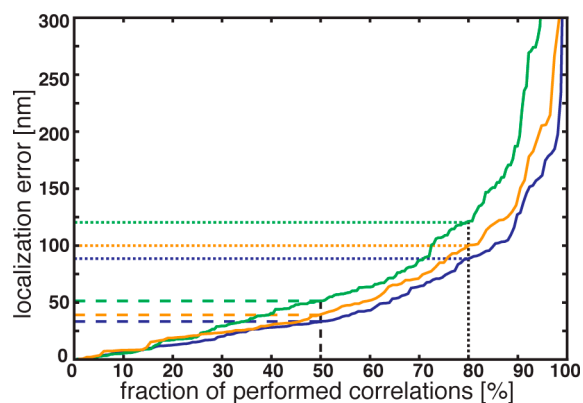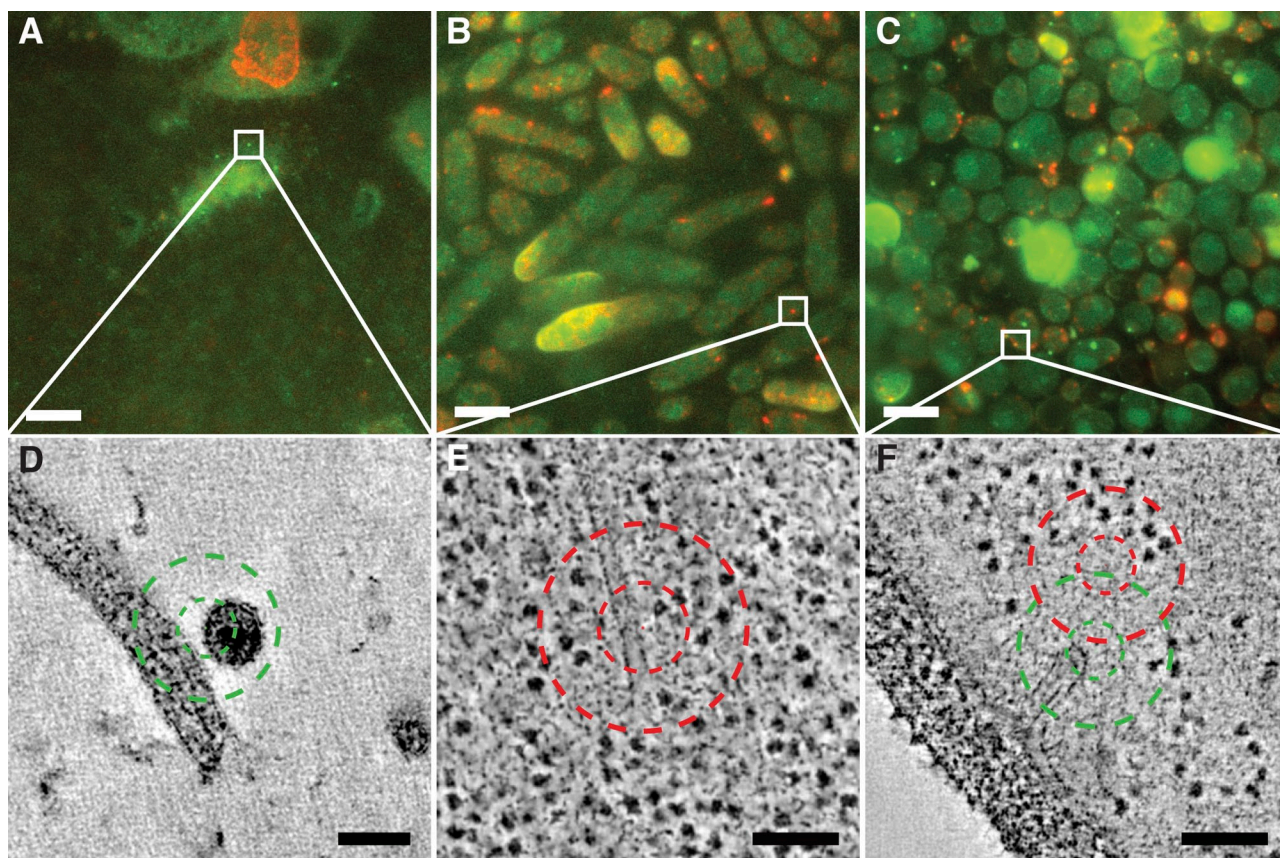
Figure 4. **Application of correlative method to three different systems.** Top panels (A–C) show fluorescence microscopy images of resin sections, merge of GFP and RFP channels. Bottom panels (D–F) are electron tomography slices of boxed areas (see also Videos 1–3). (A) HIV particles labeled with MA-EGFP on MDCK cells expressing H2B-RFP. (D) MA-EGFP–labeled HIV particles can be identified in close proximity to filopodia. (B) RFP-mal3p, GFP-atb2p expressed in *S. pombe*. (E) RFP-mal3p located at a microtubule end. (C) Rvs167-EGFP, Abp1-mCherry expressed in *S. cerevisiae*. (F) Spot of Rvs167-EGFP colocalizing with Abp1-mCherry marks an endocytic invagination of the plasma membrane. Inner and outer circles correspond to 50% and 80% prediction accuracy, whereas green and red circles stand for GFP and RFP signals, respectively. Bars: (A–C) 5 µm; (D–F) 100 nm.

plus-end (Busch and Brunner, 2004; Akhmanova and Steinmetz, 2008). We applied the method described here to investigate MTs labeled with GFP-atb2p and RFP-mal3p in fission yeast, effectively using RFP-mal3p as a label for growing MT ends. We identified mal3p-bound MT ends in the FM (Fig. 4 B) and correlated the signals with the structures of the same MT ends by ET (Fig. 4 E; Video 2). 34 isolated RFP-mal3p signals were identified in the FM, and 3D ultrastructural data of the same signals was collected using ET. 6 RFP-mal3p signals were found to be at the surface of the 300-nm section and were therefore discarded, 3 signals represented a mal3p patch within a MT bundle, and 25 signals came from MT ends, of which 16 showed flared structures, one a sheet-like structure, and 8 ambiguous structures. These results indicate that mal3p-bound, thus growing MT plus-ends, have a mostly flared morphology (Fig. 5, F–J).

Defining the time point of vesicle scission during endocytosis

As a second example, we aimed at visualizing the scission event during endocytosis in budding yeast. The dynamic organization of the endocytic machinery in budding yeast has been elucidated using live-cell imaging of fluorescent protein–labeled endocytic proteins (Kaksonen et al., 2003, 2005). Immuno-EM has been used to visualize the membrane shapes at different stages of endocytosis (Idrissi et al., 2008). However, the stages immediately before and after the vesicle scission have not been detected so far. We aimed at visualizing this defined time point during endocytosis in yeast. One component that localizes only briefly to endocytic sites at the plasma membrane is the amphiphysin Rvs167. Immuno-EM shows Rvs167 localization to the neck region of plasma membrane invaginations (Idrissi et al., 2008). We have therefore looked at a strain expressing Rvs167-EGFP together with Abp1-mCherry. In live-cell imaging, Rvs167 colocalizes transiently, for ∼10 s, with Abp1 at endocytic patches. Rvs167 is first immobile but then shows a rapid inward movement thought to correspond to vesicle scission (Kaksonen et al., 2005). In agreement with live-cell imaging, in resin sections we observed patches consisting of Abp1-mCherry only, but also patches where Rvs167-EGFP colocalized with Abp1-mCherry (Fig. 4 C). We targeted 24 sites of fluorescence colocalization by ET, 13 of which showed clear plasma membrane invaginations and 11 of which showed small vesicles (Fig. 5, K–O). Because both Abp1 and Rvs167 are present at these sites, we can conclude that the invaginations reconstructed in 3D represent endocytic sites shortly before the moment of scission (Fig. 4 F; Video 3), whereas the vesicles are imaged at a time point shortly after scission.
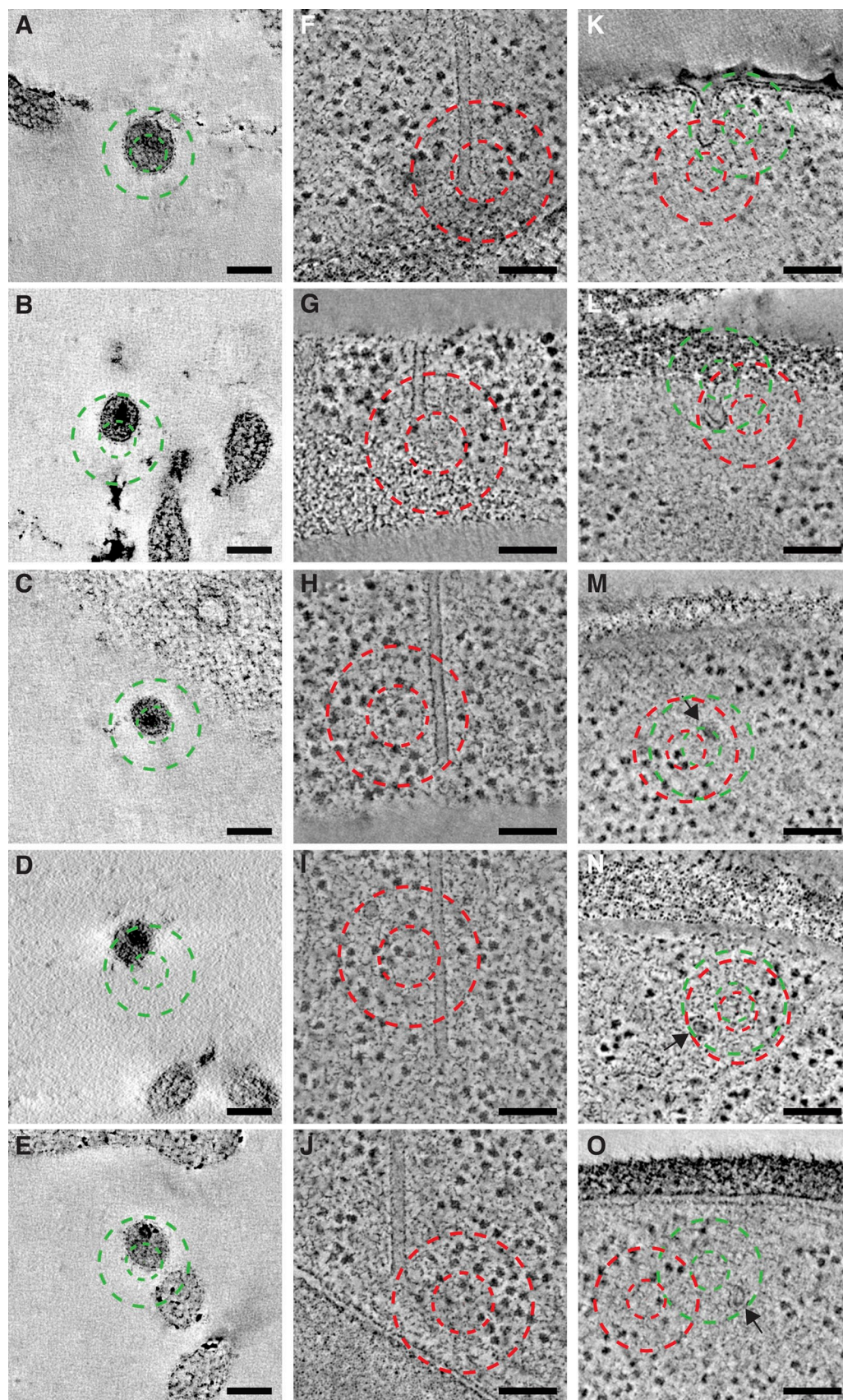
Figure 5. **Example gallery from the three different systems.** Representative ultrastructures found when targeting HIV particles labeled with MA-EGFP on MDCK cells (A–E), mal3p-RFP spots expressed in *S. pombe* (F–J), and Rvs167-EGFP colocalizing with Abp1-mCherry in *S. cerevisiae* (K–O). Inner and outer circles correspond to 50% and 80% prediction accuracy, whereas green and red circles stand for GFP and RFP signals, respectively. Bars, 100 nm.

The ratio of invaginations to vesicles suggests that scission occurs approximately halfway through the 10-s period during which these two proteins are colocalized. We have thus directly assessed the time point of vesicle scission during the Rvs167 lifetime and we have provided images of endocytic sites shortly before and after the scission moment. These results confirm that our correlative method can be used to identify specific transient intermediates in a dynamic process.

Discussion

A number of procedures for the correlation of FM and EM data have been proposed in the past few years. Methods that apply live-cell FM before preparation of the sample for EM (Müller-Reichert et al., 2007; Verkade, 2008; Kolotuev et al., 2009) rely on cryo-immobilization 5–10 s after fluorescence imaging. Although being successfully applied for controlling the developmental stage of whole organisms, or even for selecting cells that contain rare structures of interest, this approach cannot be applied to short-lived states or rapidly moving features because of the limited time resolution, and the correlation precision does not currently allow the localization of subcellular structures.

A second group of methods uses fluorescence imaging after preparation of the sample for EM. These methods have the advantage that the very same time point is imaged by FM and EM. The sample is vitrified by high pressure freezing (HPF) or plunge-freezing. It can then be imaged by FM and EM in the vitrified state, or can be freeze-substituted and embedded in resin before imaging. A recent study using a protocol for preserving GFP signals after freeze substitution and resin embedding (Nixon et al., 2009) focused on preparation techniques for zebrafish embryos and the authors were able to identify individual GFP-expressing cells within the embryo. Imaging in the vitrified state without resin embedding (cryo-EM or cryo-ET) offers high resolution, but low contrast information about the observed ultrastructures under close-to-native conditions. The need to keep the sample close to liquid nitrogen temperatures makes this approach practically challenging and hinders the use of high NA objectives that require immersion media and a short working distance (Sartori et al., 2007; Schwartz et al., 2007; Plitzko et al., 2009). This limitation means it is currently only possible to detect bright fluorescent signals and the positioning accuracy is restricted to ∼0.5 µm. Although this method can be used to locate a mitochondrion (van Driel et al., 2009), it has not been used to correlate and identify sub-organelle structures.

The potential benefits of combining FM and EM data for the study of fundamental subcellular processes can only be realized at a different scale of sensitivity and spatial precision. Here we demonstrate that the signals from FPs can be preserved in EM sections of cryofixed samples and that signals identified by FM can be reliably imaged by ET. This can be achieved with high sensitivity (∼20 GFP molecules) and high accuracy (<100 nm), permitting unambiguous localization and characterization of features such as MT ends, endocytic sites, and virus particles in different cell types.

As an initial demonstration, we have localized HIV particles among filopodia at the surface of mammalian cells, illustrating that the method can be used in studies that aim to describe rare events such as virus entry because the FM can be used to efficiently screen multiple EM grids to identify rare spots of interest. We have then applied the method to address two open cell biological questions. First, imaging of MT end structures in the presence of mal3p-RFP has allowed us to determine the morphology of individual growing MT plus-ends, showing that they are flared in vivo. This result illustrates the usefulness of the method to describe structures that adopt distinct morphologies depending on the presence or absence of auxiliary proteins. Second, we have analyzed endocytic sites in budding yeast where Rvs167 is bound. These observations reveal that vesicle scission occurs halfway through the short Rvs167 lifetime, and provides images of endocytic sites shortly before and after scission. These results exemplify the use of this method to allow imaging of transient intermediates during highly dynamic events such as vesicle scission at the plasma membrane. The high precision of localization means that these sites are unambiguously identified.

This procedure is simple, robust, and directly applicable to conventional fluorescent fusion proteins. It allows transient or rare events to be identified and described at the 1–100-nm resolution scale in the electron microscope. This capability leads to wide-ranging potential applications in cell biology.

Materials and methods

Sample preparation

S. pombe strain expressing RFP-mal3p and GFP-atb2p (gift of Stephen Huisman and Damian Brunner, EMBL, Heidelberg, Germany) and *S. cerevisiae* strains expressing EGFP- and mCherry-tagged endocytic proteins (described in Kaksonen et al., 2005) were grown in liquid YES medium and SD medium, respectively. All yeast cultures were grown at 30°C until reaching log phase, pelleted by filtering, and cryo-immobilized by HPF with a high pressure freezing system (EM PACT2; Leica).

MDCK-H2B-RFP cells (a gift of Daniela Holzer and Lars Hufnagel, EMBL, Heidelberg, Germany) were maintained in DME supplemented with 5% fetal calf serum and L-glutamine at 37°C under 5% CO_2. Cells were grown on carbon-coated sapphire disks in 24-well dishes to 60–80% confluency. Purified HIV-eGFP-delEnv particles (Müller et al., 2004; ∼250 ng p24/ well) provided by Manon Eckhardt (Universitätsklinikum Heidelberg, Heidelberg, Germany) were allowed to bind to the cell surface for 30–60 min on ice followed by cryo-immobilization by HPF with a high pressure freezing machine (HPM 010; BAL-TEC).

All samples were further processed by freeze substitution (FS) and embedding in a temperature-controlling device (model AFS2; Leica). FS occurred at −90°C for 48–58 h with 0.1% (wt/vol) uranyl acetate in glass-distilled acetone. Addition of 1–3% water, which is in some cases desired to improve membrane contrast (Walther and Ziegler, 2002), was tested and did not influence fluorescence retention. The temperature was then raised to −45°C (5°C/hour), and samples were washed with acetone and infiltrated with increasing concentrations (10, 25, 50, and 75%; 4 h each) of Lowicryl in acetone while the temperature was further raised to −25°C. 100% Lowicryl was exchanged three times in 10-h steps and samples were UV polymerized at −25°C for 48 h, after which the temperature was raised to 20°C (5°C/hour) and UV polymerization continued for 48 h. 300-nm sections were cut with a microtome (Ultracut UCT; Leica) and a diamond knife and picked up on carbon-coated 200 mesh copper grids. Blue (365 nm/415 nm) 0.02 µm FluoSpheres (Invitrogen) were pretreated (to reduce intensity) with 0.1% Tween 20 for 10 min, washed twice by ultracentrifugation at 100,000 g, resuspended in PBS, and adsorbed to the EM grids by placing the grids section face-down onto a 15-µl drop of FluoSpheres for 10 min. Grids were then washed with three drops of water and blotted with filter paper.

Fluorescence microscopy and imaging

For live-cell microscopy of yeast, cells were adhered to concanavalin A–coated (0.1 µl/ml) circular coverslips (25-mm diameter) placed in a

custom-made holder and imaged in SD medium. For conventional FM of MDCK cells with bound HIV-1, cells were fixed with 4% PFA in PBS and embedded in Mowiol.

For imaging of EM grids, the grid was placed on a 25–30-µl drop of water on a circular coverslip (Fig. S2). The sandwich was closed with a second coverslip that had a layer of vacuum grease at the rim, preventing drying and hence sticking of the resin sections to the glass. During imaging, the section side of the EM grid was facing toward the objective. The water layer between section and coverslip ensured optimal imaging conditions by allowing the use of oil immersion objectives. While regions of interest were imaged, their positions on the grid (i.e., relative to the gridsquares) were recorded and could be easily found back by EM. This could be facilitated by use of commercially available "finder" EM grids with labeled grid regions, but we have not found this necessary. All imaging was done at room temperature using a microscope (model IX81; Olympus) equipped with a 100x NA 1.45 objective, a camera (Orca-ER; Hamamatsu Photonics), and electronic shutters and filter wheels (Sutter Instrument Co.). FM was done with a lamp (X-Cite 120PC; EXFO Life Sciences) using 470/22-nm, 556/20-nm, and 377/50-nm filters for excitation of GFP, mCherry, and Blue FluoSpheres, respectively. Emission was imaged using a 520/35-nm filter for GFP, a 624/40-nm filter for mCherry, and a 520/35-nm filter for Blue FluoSpheres. The CCD camera, filter wheels, and shutters were controlled by MetaMorph software (Universal Imaging Corp.). Because the imaged section area was not perfectly flat, several images at different focal planes were taken per channel.

Electron tomography

Grids with yeast sections were post-stained with Reynolds lead citrate for contrast enhancement, whereas grids with MDCK sections were left unstained. 15-nm protein A–coupled gold beads were adsorbed on both sides of all grids as tomographic-fiducial markers. Grids were placed in a high-tilt holder (Model 2020; Fischione Instruments), and digital images were recorded on a camera (4k Eagle; FEI) as dual-axis tilt series over a −60° to 60° tilt range (1° increment) on a microscope (Tecnai TF30; FEI) operated at 300 kV. Pixel sizes were typically 1.18 nm (*S. pombe* and *S. cerevisiae*), 1.52 nm or 1.97 nm (MDCK cells) at the specimen level. Lower magnification tilt series for FluoSpheres-based correlation were collected as single-axis tilt series at 2.53-nm or 5.07-nm pixel size and at 3° or 2° increment, respectively. Tomograms were reconstructed using the IMOD software package (version 3.13.2; Kremer et al., 1996).

Fiducial-based correlation

We tested Quantum Dots, Rhodamine-labeled gold particles, and FluoSpheres as possible fiducial markers and found the latter to perform best. The concentration of fiducials was adjusted to obtain a distribution density low enough that they were clearly resolved from one another in the FM, but high enough that ∼6–10 fiducials fell within the region reconstructed in the electron tomogram. If the structure of interest required very high magnification at the ET level and thus not enough FM-resolved fiducials were present in the tomogram, a lower magnification tomogram was collected to perform the correlation.

To visualize all fiducials in one EM image, tomogram slices showing the fiducials adhered to the section surface were averaged. Fiducial pairs were selected in the averaged EM image and the corresponding fluorescent image of the fiducials using MATLAB (The MathWorks, Inc.). Centroid positions of selected fiducials in both images were localized by sub-pixel accuracy centroid fit. To localize the centroid position of the FP spot, a high-pass filter was applied to reduce the effect of gradients in the cellular background before sub-pixel fitting (Fig. 2 A, inset). From the measured coordinates, transformations based on all possible subset combinations of fiducial pairs were computed. The transformations were scored by comparing the sum of squared residuals of the predicted fiducial positions from the coordinates of fiducial centroids in the EM image, and the best-scoring transform was used for transformation of the coordinates of the spot of interest onto the electron tomogram. This approach avoids inaccurate correlations due to outlier fiducials, caused by, e.g., local deteriorations of the sections.

To account for drift between the fiducial fluorescence image and the GFP or RFP image, fiducials that show bleed-through into the channel of interest were selected and the average shift between the two channels was calculated and corrected for. Broad wavelength fiducials (Tetraspecks), which also fluoresce in the channel of interest, can also be used. Alternatively, we found that stage-derived drift can be prevented by using a nose-piece stage.

Where a higher magnification tomogram was collected, the transform between low and high magnification tomograms was calculated analogously using the gold beads used for tomographic reconstruction as

fiducial markers, and the FP centroid coordinates were transformed further using the resulting transform.

Accuracy estimation

By omitting each fiducial once and calculating the optimal transformation based on the remaining fiducials, the position of the omitted fiducial was predicted and its predicted coordinates compared with its true position. This procedure provided a prediction accuracy value for each fiducial representing one optimal transformation. This calculation was performed for all transformations in each one of the three datasets. Merged results are displayed in Fig. 3 as fraction of the total set of transformations against the corresponding prediction accuracy. The datasets comprise 218 fiducials for *S. pombe*, 116 for MDCK cells, and 158 for *S. cerevisiae*.

Online supplemental material

Fig. S1 shows preservation of fluorescent signal of Rvs167-EGFP. Fig. S2 shows setup for imaging resin sections on EM grids by FM. Video 1 shows EGFP-labeled HIV particle at the cell surface of MDCK cells. Video 2 shows flared MT end structure decorated with RFP-mal3p in *S. pombe*. Video 3 shows endocytic invagination at the *S. cerevisiae* plasma membrane in the presence of Rvs167-EGFP and Abp1-mCherry. Online supplemental material is available at http://www.jcb.org/cgi/content/full/jcb.201009037/DC1.

References

Akhmanova, A., and C.C. Hoogenraad. 2005. Microtubule plus-end-tracking proteins: mechanisms and functions. *Curr. Opin. Cell Biol.* 17:47–54. doi:10.1016/j.ceb.2004.11.001

Akhmanova, A., and M.O. Steinmetz. 2008. Tracking the ends: a dynamic protein network controls the fate of microtubule tips. *Nat. Rev. Mol. Cell Biol.* 9:309–322. doi:10.1038/nrm2369

Busch, K.E., and D. Brunner. 2004. The microtubule plus end-tracking proteins mal3p and tip1p cooperate for cell-end targeting of interphase microtubules. *Curr. Biol.* 14:548–559. doi:10.1016/j.cub.2004.03.029

Chlanda, P., M.A. Carbajal, M. Cyrklaff, G. Griffiths, and J. Krijnse-Locker. 2009. Membrane rupture generates single open membrane sheets during vaccinia virus assembly. *Cell Host Microbe.* 6:81–90. doi:10.1016/j.chom.2009.05.021

Chrétien, D., S.D. Fuller, and E. Karsenti. 1995. Structure of growing microtubule ends: two-dimensional sheets close into tubes at variable rates. *J. Cell Biol.* 129:1311–1328. doi:10.1083/jcb.129.5.1311

Höög, J.L., C. Schwartz, A.T. Noon, E.T. O'Toole, D.N. Mastronarde, J.R. McIntosh, and C. Antony. 2007. Organization of interphase microtubules in fission yeast analyzed by electron tomography. *Dev. Cell.* 12:349–361. doi:10.1016/j.devcel.2007.01.020

Idrissi, F.-Z., H. Grötsch, I.M. Fernández-Golbano, C. Presciatto-Baschong, H. Riezman, and M.-I. Geli. 2008. Distinct acto/myosin-I structures associate with endocytic profiles at the plasma membrane. *J. Cell Biol.* 180:1219–1232.

Joglekar, A.P., D.C. Bouck, J.N. Molk, K.S. Bloom, and E.D. Salmon. 2006. Molecular architecture of a kinetochore-microtubule attachment site. *Nat. Cell Biol.* 8:581–585. doi:10.1038/ncb1414

Kaksonen, M., Y. Sun, and D.G. Drubin. 2003. A pathway for association of receptors, adaptors, and actin during endocytic internalization. *Cell.* 115:475–487. doi:10.1016/S0092-8674(03)00883-3

Kaksonen, M., C.P. Toret, and D.G. Drubin. 2005. A modular design for the clathrin- and actin-mediated endocytosis machinery. *Cell.* 123:305–320. doi:10.1016/j.cell.2005.09.024

Kolotuev, I., Y. Schwab, and M. Labouesse. 2009. A precise and rapid mapping protocol for correlative light and electron microscopy of small invertebrate organisms. *Biol. Cell.* 102:121–132. doi:10.1042/BC20090096

Kremer, J.R., D.N. Mastronarde, and J.R. McIntosh. 1996. Computer visualization of three-dimensional image data using IMOD. *J. Struct. Biol.* 116:71–76. doi:10.1006/jsbi.1996.0013

Luther, P.K., M.C. Lawrence, and R.A. Crowther. 1988. A method for monitoring the collapse of plastic sections as a function of electron dose. *Ultramicroscopy.* 24:7–18. doi:10.1016/0304-3991(88)90322-1

Müller, B., J. Daecke, O.T. Fackler, M.T. Dittmar, H. Zentgraf, and H.-G. Kräusslich. 2004. Construction and characterization of a fluorescently labeled infectious human immunodeficiency virus type 1 derivative. *J. Virol.* 78:10803–10813. doi:10.1128/JVI.78.19.10803-10813.2004

Müller-Reichert, T., M. Srayko, A. Hyman, E.T. O'Toole, and K. McDonald. 2007. Correlative light and electron microscopy of early *Caenorhabditis elegans* embryos in mitosis. *Methods Cell Biol.* 79:101–119. doi:10.1016/S0091-679X(06)79004-5

Nixon, S.J., R.I. Webb, M. Floetenmeyer, N. Schieber, H.P. Lo, and R.G. Parton. 2009. A single method for cryofixation and correlative light, electron microscopy and tomography of zebrafish embryos. *Traffic.* 10:131–136. doi:10.1111/j.1600-0854.2008.00859.x

O'Toole, E.T., M. Winey, and J.R. McIntosh. 1999. High-voltage electron tomography of spindle pole bodies and early mitotic spindles in the yeast *Saccharomyces cerevisiae. Mol. Biol. Cell.* 10:2017–2031.

O'Toole, E.T., K.L. McDonald, J. Mäntler, J.R. McIntosh, A.A. Hyman, and T. Müller-Reichert. 2003. Morphologically distinct microtubule ends in the mitotic centrosome of *Caenorhabditis elegans. J. Cell Biol.* 163:451–456. doi:10.1083/jcb.200304035

Plitzko, J.M., A. Rigort, and A. Leis. 2009. Correlative cryo-light microscopy and cryo-electron tomography: from cellular territories to molecular landscapes. *Curr. Opin. Biotechnol.* 20:83–89. doi:10.1016/j.copbio.2009.03.008

Sartori, A., R. Gatz, F. Beck, A. Rigort, W. Baumeister, and J.M. Plitzko. 2007. Correlative microscopy: bridging the gap between fluorescence light microscopy and cryo-electron tomography. *J. Struct. Biol.* 160:135–145. doi:10.1016/j.jsb.2007.07.011

Schwartz, C.L., V.I. Sarbash, F.I. Ataullakhanov, J.R. McIntosh, and D. Nicastro. 2007. Cryo-fluorescence microscopy facilitates correlations between light and cryo-electron microscopy and reduces the rate of photobleaching. *J. Microsc.* 227:98–109. doi:10.1111/j.1365-2818.2007.01794.x

van Driel, L.F., J.A. Valentijn, K.M. Valentijn, R.I. Koning, and A.J. Koster. 2009. Tools for correlative cryo-fluorescence microscopy and cryo-electron tomography applied to whole mitochondria in human endothelial cells. *Eur. J. Cell Biol.* 88:669–684. doi:10.1016/j.ejcb.2009.07.002

van Rijnsoever, C., V. Oorschot, and J. Klumperman. 2008. Correlative light-electron microscopy (CLEM) combining live-cell imaging and immunolabeling of ultrathin cryosections. *Nat. Methods.* 5:973–980. doi:10.1038/nmeth.1263

Verkade, P. 2008. Moving EM: the Rapid Transfer System as a new tool for correlative light and electron microscopy and high throughput for high-pressure freezing. *J. Microsc.* 230:317–328. doi:10.1111/j.1365-2818.2008.01989.x

Walther, P., and A. Ziegler. 2002. Freeze substitution of high-pressure frozen samples: the visibility of biological membranes is improved when the substitution medium contains water. *J. Microsc.* 208:3–10. doi:10.1046/j.1365-2818.2002.01064.x